Cationic Polaron Delocalization in Porphyrin Nanoribbons

Sebastian M. Kopp,[1,2] Jie-Ren Deng,[2] Ashley J. Redman,[1] Henrik Gotfredsen,[2] Robert M. J. Jacobs,[2] Harry L. Anderson,[2,*] and Christiane R. Timmel[1,2,3**]

[1]Centre for Advanced Electron Spin Resonance, Department of Chemistry, University of Oxford, Oxford, OX1 3QR, UK

[2]Chemsitry Research Laboratory, Department of Chemistry, University of Oxford, Oxford, OX1 3TA, UK

[3]Lead contact

*Correspondence: harry.anderson@chem.ox.ac.uk

**Correspondence: christiane.timmel@chem.ox.ac.uk

SUMMARY

Long-range delocalization of unpaired electrons in organic π-conjugated oligomers is an important requirement to achieve high charge carrier mobilities in molecular transistors. We have investigated the polaron delocalization in the radical cations of a series of β,*meso*,β-edge-fused porphyrin oligomers consisting of up to 18 porphyrin units by a combination of cw-EPR, ^{1}H and ^{14}N ENDOR, HYSCORE and vis-NIR-MIR spectroscopy, supported by DFT simulations. The results demonstrate coherent delocalization of the radical cation over more than ten porphyrin units, which corresponds to an effective coherence length >8.5 nm. We discovered a remarkably non-uniform distribution of the radical spin density and an increase in phase memory time with increasing delocalization length (up to $T_m \approx 4$ µs at 50 K). This study opens new avenues towards the design of molecular electronic and spintronic materials.

Key words: porphyrin tapes, delocalization, polarons, electron paramagnetic resonance, spectroelectrochemistry, organic polymers, nanoribbons

INTRODUCTION

The one-electron oxidation of a π-conjugated polymer to its radical cation results in a reorganization, or polarization, of the molecular framework and solvent environment.[1-3] This combination of the unpaired electron, positive charge and associated structural changes comprise a hole polaron.[4] Maximizing the polaron spatial coherence lengths is essential for the design of organic semiconductors for efficient charge transport in organic solar cells and field-effect transistors.[5-12] In addition, organic polymers with long coherence times and extended polaron delocalization are promising building blocks to sustain spin-polarized currents in molecular spintronics,[13-16] and for fabricating single-molecule electronic devices. Charge transport through an electrode/molecule/electrode junction can either occur by direct tunneling or via multistep hopping.[17,18] The former mechanism is favored by polaron states delocalized over the entire molecule.[19] Porphyrin-based molecular wires with ethyne-links between their *meso* positions have been found to exhibit long-range radical delocalization, with negative polarons spanning 7 porphyrin units (~7.5 nm) and positive polarons delocalized over 5 porphyrin units (~5.6 nm).[20-23] This efficient polaron delocalization result in high single-molecule conductance.[16,24,25] The edge-fused porphyrin oligomers pioneered by Osuka are another promising class of molecular wires due to their steeply decreasing π-π^* energy gaps with increasing oligomer length and the shallow length-dependence of their molecular conductance.[26-32] Recent work has shown that these porphyrin nanoribbons exhibit phase-coherent charge-transport over eight porphyrin units in single-molecule transistors.[19] This has sparked interest in the extent of polaron delocalization in this family of molecular wires.

In this work, we have used a combination of continuous wave EPR, ^{1}H and ^{14}N Mims electron-nuclear double resonance (ENDOR) spectroscopy, ^{14}N hyperfine sublevel correlation (HYSCORE) spectroscopy, visible-NIR-MIR spectroelectrochemistry, and supporting DFT calculations and simulations to probe the radical cation delocalization in a family of porphyrin nanoribbons with up to 18 porphyrin units. Our analysis demonstrates coherent polaron delocalization over more than ten porphyrin units (> 8.5 nm) which marks the longest coherently delocalized polaron reported in π-conjugated materials to date.[20,22,33]

RESULTS
Synthesis of Porphyrin Oligomers
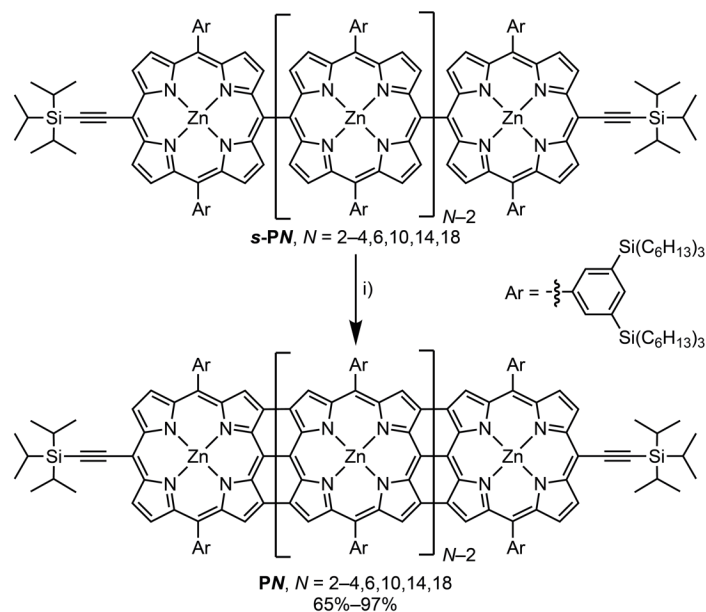
Scheme 1. Synthesis of edge-fused porphyrin oligomers
Synthesis of β,*meso*,β-triply linked oligomers **PN** N = 2–4, 6, 8, 10, 14, 18 from their singly linked precursors **s-PN**; i) 2,3-dichloro-5,6-dicyano-*p*-benzoquinone (DDQ), Sc(OTf)$_3$, toluene, 80 °C, 2 h; see SI Scheme S1 for the complete synthesis.

Meso-meso singly linked porphyrin oligomers with different lengths were synthesized by a combination of silver-mediated oxidative coupling and nickel-mediated Yamamoto coupling, and purified by recycling gel-permeation chromatography. Bromination of the terminal *meso* positions of each oligomer, followed by Sonogashira coupling to attach the terminal triisopropylsilyl (TIPS) acetylenes, gave the corresponding porphyrin oligomers **s-PN** (N = 2–4, 6, 10, 14, 18) (SI Scheme S1). The role of the terminal TIPS-acetylene units is to protect the ends of the chain during oxidative fusion and to enhance solubility. Subjection of **s-PN** to oxidative fusion conditions with DDQ and Sc(OTf)$_3$ at 80 °C under argon for 2 hours afforded the β,*meso*,β-triply linked oligomers **PN** in good to excellent yields (Scheme 1). Monomer **P1** was synthesized as a reference compound following published procedures.[34] Bulky 3,5-bis(trihexylsily)phenyl substituents were attached to both peripheral *meso* positions of each porphyrin unit to improve the solubility of the fused porphyrin oligomers in common organic solvents such as toluene, and to inhibit aggregation. The oxidative fusion reactions of oligomers bearing TIPS-acetylenes at the terminal *meso* positions were exceptionally efficient, no demetallation and partially fused products were identified from the UV-vis-NIR spectra of the products after the reaction. Partial oxidation of **PN** to the radical monocations **PN**$^{\bullet+}$ was achieved by addition of 0.5 equivalents tris(4-bromophenyl)-aminium hexachloroantimonate (BAHA) in a 1:1:1 solvent mixture of CD$_2$Cl$_2$:toluene-d_8:THF-d_8, which forms a glass at low temperatures.[22,35]

Continuous Wave EPR

The room temperature cw-EPR spectra of the radical cations **P1**$^{\bullet+}$ to **P4**$^{\bullet+}$, **P6**$^{\bullet+}$, and **P10**$^{\bullet+}$ at X-band frequencies are shown in Figure 1A. The spectrum of **P1**$^{\bullet+}$ is consistent with those previously reported for similar monomer cations.[22,35] The nine prominent hyperfine lines in the spectrum arise from an isotropic coupling of $^{14}\text{N}A_{\text{iso}}$ = 4.07 MHz to the four equivalent ^{14}N nuclei of the porphyrin and are further split by an isotropic hyperfine coupling of about $^{1}\text{H}A_{\text{iso}}$ = 1.0 MHz to the four equivalent *ortho*-protons on the aryl rings. The spectrum of **P2**$^{\bullet+}$ also shows a partially resolved hyperfine pattern that arises from coupling to the eight ^{14}N nuclei, whereas the longer oligomers lack a resolved hyperfine structure due to substantial inhomogeneous broadening. If hyperfine interactions are the main contribution to the spectral envelope width ΔB_N and the radical spin-density is completely and uniformly delocalized, the theoretical relationship in equation 1 established by Norris *et al.* can be applied to determine the delocalization length in the series of porphyrin nanoribbons **PN**$^{\bullet+}$:

$$\Delta B_N = \frac{1}{\sqrt{N}}\Delta B_{N=1} \tag{1}$$

2

where N is the number of porphyrin units in an oligomer and $\Delta B_{N=1}$ is the spectral envelope width of the monomer spectrum.[36] Here, complete and uniform delocalization refers to an equal amount of spin-density on each porphyrin unit in a chain with an identical distribution of this spin-density within the porphyrin units. The spectral envelope widths of $\mathbf{P}N^{\bullet+}$ were determined by fitting the first derivative of a Gaussian or Lorentzian distribution to the cw-EPR spectra (SI Figures S4, S5). For $N \leq 10$, the lineshapes of all cw-EPR spectra are best described by a Gaussian envelope, which indicates that the main contribution to the spectral shape arises from unresolved hyperfine couplings.
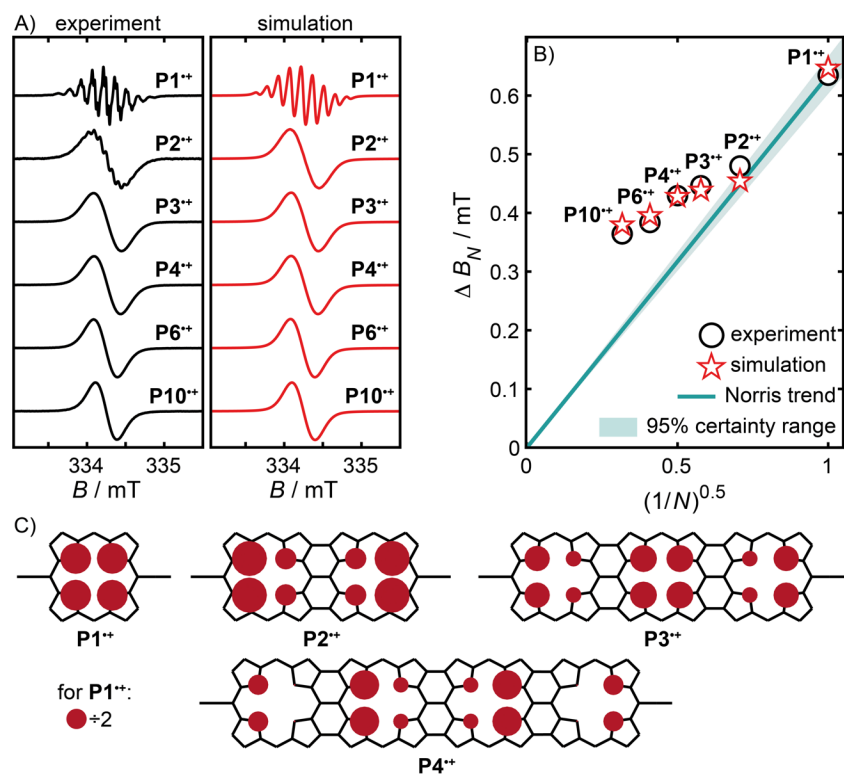

Figure 1. X-band cw-EPR spectroscopy
(A) (Left) Experimental cw-EPR spectra of the radical cations $\mathbf{P}N^{\bullet+}$ (N = 1–4, 6, 10) acquired at 298 K in CD$_2$Cl$_2$:toluene-d_8:THF-d_8 1:1:1 at X-band frequencies. (Right) Simulated cw-EPR spectra of $\mathbf{P}N^{\bullet+}$ using the isotropic ^{14}N hyperfine couplings ^{14}NA_{iso} derived from a distributed point-dipole calculation. (B) Comparison of the experimental and simulated Gaussian envelop widths ΔB_N vs $(1/N)^{1/2}$. (C) Schematic representation of the isotropic ^{14}N hyperfine interactions in $\mathbf{P}N^{\bullet+}$ N = 1–4 used to simulate the cw-EPR spectra. The radius of the red sphere on each nucleus is proportional to the magnitude of ^{14}NA_{iso}; for $\mathbf{P}1^{\bullet+}$ the shown radius is divided by two for clarity. Aryl and silyl solubilizing groups are omitted for clarity; see SI Figure S8 for the isotropic hyperfine visualization for N = 6 and 10.

The Gaussian spectral envelop widths, ΔB_N, of $\mathbf{P}N^{\bullet+}$ (N = 1–4, 6, 10) are compared to equation 1 in Figure 1B. Although the width of the cw-EPR spectra for the series continuously decreases with increasing oligomer length, the experimental envelope widths deviate from the ideal values predicted by Norris by up to ~90%. As discussed in detail by Moise et al.,[22] it is necessary that the inherent line width Γ_N of the EPR transitions remains constant (and small) throughout an oligomer series for equation 1 to be applicable. Previous studies of the radical cations of butadiyne- and ethyne-linked porphyrin oligomers have shown that Γ_N remains approximately constant and similar to Γ_1.[22,35] However, the increased rigidity and length of the porphyrin backbone in $\mathbf{P}N^{\bullet+}$ might lead to relevant changes in the rotational correlations times and consequently Γ_N as a function of oligomer size and warrants further investigation. If complete and uniform spin delocalization ($A_N = A_{N=1}/N$) is imposed in the numerical simulation of the cw-EPR spectra of $\mathbf{P}N^{\bullet+}$, the inherent line width Γ_N required to fit the spectra increases discontinuously with the largest changes in Γ_N occurring in oligomers with $N \leq 4$ (SI Figure S6). This observation is not in agreement with a continuously increasing line width Γ_N with increasing oligomer length expected if changes in the rotational correlation time were behind the experimental trend in Figure 1B. Simulations of the cw-EPR spectra of $\mathbf{P}N^{\bullet+}$ with a constant Lorentzian line width Γ_N = 0.07 mT and the isotropic component ^{14}NA_{iso} of the ^{14}N hyperfine interaction calculated with a distributed point-dipole model for completely delocalized spin density distributions (*vide infra*) provide an excellent agreement with the experimental spectra and replicate the trend in the experimental spectral widths (Figure 1A+B). Importantly, the isotropic hyperfine interactions used in these simulations are not equal for all ^{14}N

3

nuclei. Instead, a non-uniform distribution of ^{14}N hyperfine interactions spanning all porphyrin units in each oligomer results in the excellent agreement with the experimental spectra (Figure 1C and SI Figure S8).

To determine whether additional spin density distributions predicted by DFT can also describe the electronic structure of $PN^{\bullet+}$, their cw-EPR spectra were simulated following an approach by Moise *et al.*[22]: the isotropic nitrogen hyperfine interactions $^{14}N A_{iso}$ used in the simulations were obtained by multiplying the DFT predicted ^{14}N spin populations for $N > 1$ with the McConnell constant calculated as the proportionality factor between $^{14}N A_{iso}$ and the ^{14}N spin populations in $P1^{\bullet+}$ (see SI Section 3.4).[22,37] Calculations with the B3LYP functional predict a non-uniform distribution of radical spin density over at least ten porphyrin units in $PN^{\bullet+}$. These spin densities give simulated cw-EPR spectra that are in excellent agreement with the experiment (SI Figure S7) and were used to guide the spin density distributions behind the point-dipole calculations (*vide infra*). The influence of the DFT functional on the calculated spin densities and subsequent cw-EPR simulations was investigated by screening additional functionals with different range-separation parameters and Hartree–Fock exchange, which strongly influence the predicted electron delocalization.[38-40] All simulations that result in a close agreement with the experimental cw-EPR spectra are based on similar spin densities to the ones found with B3LYP, whereas different spin density distributions result in stark deviations from the experiment (SI Figure S7). This further strengthens the validity of the Mulliken populations calculated at the B3LYP level and suggest that the deviation from equation 1 in Figure 1B results from the non-uniform spin distribution in the porphyrin nanoribbons with approximately equal amounts of spin density on each porphyrin unit and a remarkably different distribution of this spin density in the individual porphyrins (see SI Section 2). The average non-uniformity of the spin densities in $PN^{\bullet+}$ is substantially larger than for previously investigated butadiyne- and ethyne-linked porphyrin oligomers, which suggests that oligomers with stronger porphyrin-porphyrin electronic coupling exhibit more pronounced non-uniform spin distributions (SI Figure S2, Table S2). The spectral widths for $P14^{\bullet+}$ and $P18^{\bullet+}$ show an abrupt increase and deviate substantially from the trend observed for their shorter analogues (SI Figure S4). This is probably the result of significant anisotropic broadening, due to the slow tumbling of these long, rigid, rod-shaped molecules in solution, and prevents a more detailed analysis of their cw-EPR spectra in comparison to their shorter counterparts.

W-band Pulsed EPR

Low-temperature Spectra
The W-band echo-detected field sweep spectra of $PN^{\bullet+}$ (N = 1–4, 6, 10) measured in frozen solution at 50 K are consistent with a rhombic g-tensor with small anisotropy as expected for organic π-radicals (SI Figure S9, Table S5).[41,42] Supporting DFT calculations are qualitatively consistent with the experimentally determined g-tensors and predict an alignment to the tensor principle axes with the out-of-plane axis (g_z), the axis along the aryl solubilizing sidechains (g_y), and the long axis of $PN^{\bullet+}$ defined by the β,*meso*,β-triply fused motives (g_x).
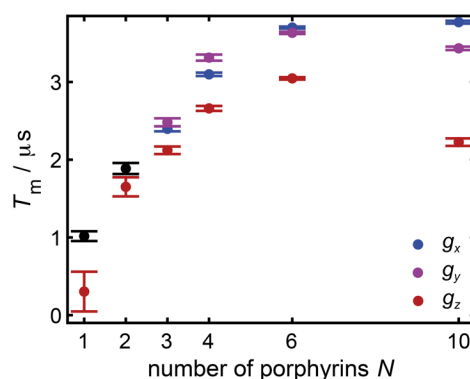

Figure 2. Phase memory time
Comparison of the phase memory coherence times T_m of $PN^{\bullet+}$ (N = 1–4, 6, 10) at 50 K in CD$_2$Cl$_2$:toluene-d_8:THF-d_8 1:1:1 performed at magnetic fields corresponding to the principal values g_x, g_y, and g_z of the anisotropic g-tensors. For $P1^{\bullet+}$ and $P2^{\bullet+}$ the g_x and g_y field positions are not sufficiently resolved in the experimental spectra and the reported coherence times correspond to $g_{x,y}$. The error margins show a 95% confidence interval of the fitted T_m values.

All porphyrin oligomer cations show a field dependence of their phase memory times T_m at 50 K with longer coherence times observed at the field positions corresponding to g_x and g_y (Figure 2). Anisotropic relaxation times have been reported in the literature for a variety of systems and were attributed to decoherence originating from changes in the effective g-values through molecular motion.[43-45] We suggest that libration in the porphyrin xy-plane dominate the relaxation processes in $PN^{\bullet+}$ at 50 K as T_m is typically longest along the axis of molecular motion.[43] Noticeably, the phase memory times of $PN^{\bullet+}$, N = 1–4, 6, 10, continuously increase with increasing chain length under identical acquisition conditions, as exemplified by the more than threefold increase in the phase

4

memory time at the g_x field position from 1.0 µs for **P1$^{\bullet+}$** to 3.8 µs for **P10$^{\bullet+}$**. This trend could be explained by smaller perturbations of the radical coherence via nuclear-spin diffusions due to smaller anisotropic hyperfine interactions in the longer oligomers.

Mims ENDOR Spectroscopy and Hyperfine Coupling Calculations

The anisotropic ^{1}H and ^{14}N hyperfine interactions of **PN$^{\bullet+}$** were determined by pulse Mims ENDOR spectroscopy in frozen solutions at 50 K. Although decomposition of the Mims ENDOR spectra is not feasible due to the large number of nuclei with similar hyperfine couplings that contribute to the spectra, they still provide valuable insight into the electronic structure of the porphyrin radical cations: Dynamic polaron migration or electron hopping can occur rapidly on the EPR time-scale at room temperature and can therefore contribute to the apparent spin density distribution.[46] However, these processes are typically not observed by EPR spectroscopy at cryogenic temperatures in a frozen matrix providing a better probe of the radical delocalization.[22,35] In addition, due to the lack of dynamical averaging in a frozen solvent matrix the anisotropic hyperfine interactions may be resolved and ENDOR measurements provide additional information beyond what can be obtained from cw-EPR spectroscopy in the isotropic limit.
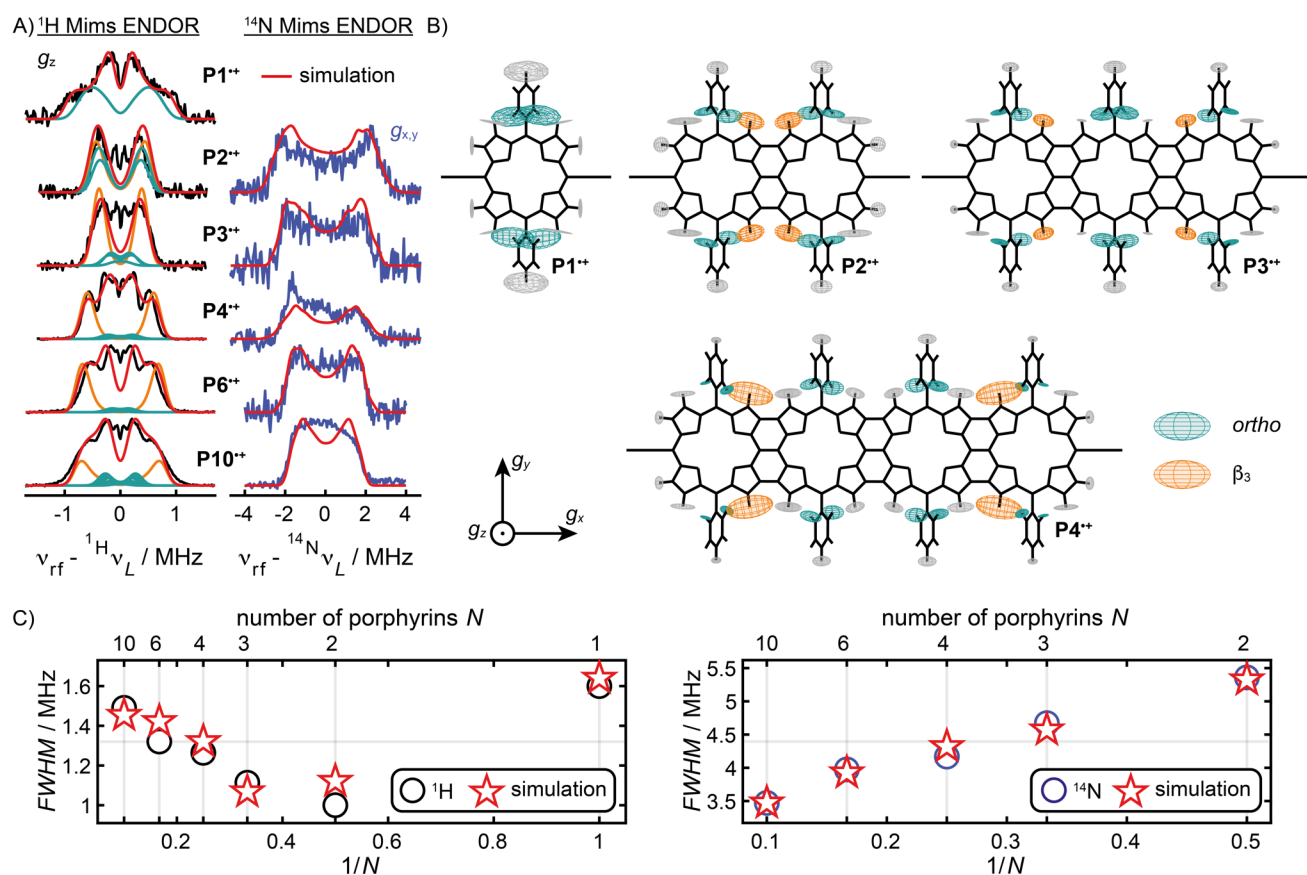

Figure 3. W-band ^{1}H and ^{14}N Mims ENDOR spectroscopy

(A) ^{1}H (black) and ^{14}N (blue) Mims ENDOR spectra of **PN$^{\bullet+}$** acquired at 50 K in frozen CD$_2$Cl$_2$:toluene-d_8:THF-d_8 1:1:1 at W-band frequencies together with their simulations (red) using anisotropic hyperfine tensors derived from distributed point-dipole calculations. The individual contributions to the ^{1}H Mims ENDOR spectra from the *ortho*- and β_3-hydrogens are highlighted in green and orange, respectively. The ^{1}H and ^{14}N ENDOR spectra were measured at field positions corresponding to g_z and $g_{x,y}$, respectively. (B) Schematic representation of the anisotropic ^{1}H hyperfine tensors ^{1H}A of **PN$^{\bullet+}$** $N = 1$–4 shown as ellipsoids centered at the corresponding ^{1}H nuclei with dimensions proportional to the eigenvalues of ^{1H}A and are oriented in the molecular frame based on their Euler angles. The tensors of the *ortho*- and β_3-protons that give rise to the highlighted contributions in (A) are shown in green and orange; additional tensors are shown in grey as reference; see SI Figure S22 for the hyperfine visualization for $N = 6$ and 10. (C) Trend of the full width at half maximum (*FWHM*) of the experimental and simulated ENDOR spectra.

The W-band ^{1}H and ^{14}N Mims ENDOR spectra of **P$N^{\bullet+}$** (N = 1–4, 6, 10) are shown in Figure 3A. The proton spectra presented here were measured at the field positions corresponding to g_z and are complemented by a detailed analysis of the ^{1}H ENDOR spectra measured at the $g_{x,y}$ field position in Section 4.4 of the Supplemental Information. All ^{1}H and ^{14}N ENDOR spectra are centered at the Larmor frequency of the relevant nucleus and split into symmetric peaks by the hyperfine interactions. This is characteristic for nuclei in the weak coupling limit with smaller hyperfine couplings than the Larmor frequency ($A < 2\nu$). Hyperfine spectroscopy is a powerful tool to probe the spin distribution of organic π-radicals. The magnitude of the individual hyperfine interactions, and consequently the width of the ENDOR signal, decreases for an increasingly delocalized radical (although the total number of hyperfine interactions increases) if the delocalization does not result in substantial changes to the hyperfine anisotropies.[36] The trend in width of the experimental ENDOR spectra of **P$N^{\bullet+}$** as a function of oligomer length is shown in Figure 3C with the full width at half maximum (*FWHM*) as measure of the experimental spectral width. The *FWHM* of the ^{14}N ENDOR spectra continuously decreases for N = 2–10 which indicates a sustained decrease of the largest ^{14}N hyperfine interaction (which determines the *FWHM*) consistent with coherent delocalization of the radical spin density over at least ten porphyrin units in **P$N^{\bullet+}$**. The *FWHM* of the ^{1}H ENDOR spectra initially decreases for N = 1–2 as expected for an increasingly delocalized radical. Surprisingly, this trend is inverted for N = 3–10, with a continuously increasing *FWHM* accompanied by the emergence of a clearly resolved shoulder in the ^{1}H ENDOR spectra in Figure 3A. Analogous behavior is found for the ^{1}H ENDOR spectra measured at the $g_{x,y}$ field position (SI Figures S19, S20) in stark contrast to the ^{14}N ENDOR results and previous reports on ethyne- and butadiyne-linked porphyrin radical cations, which exhibit continuously narrowing ^{1}H ENDOR widths until their effective polaron delocalization lengths are reached.[22,35]
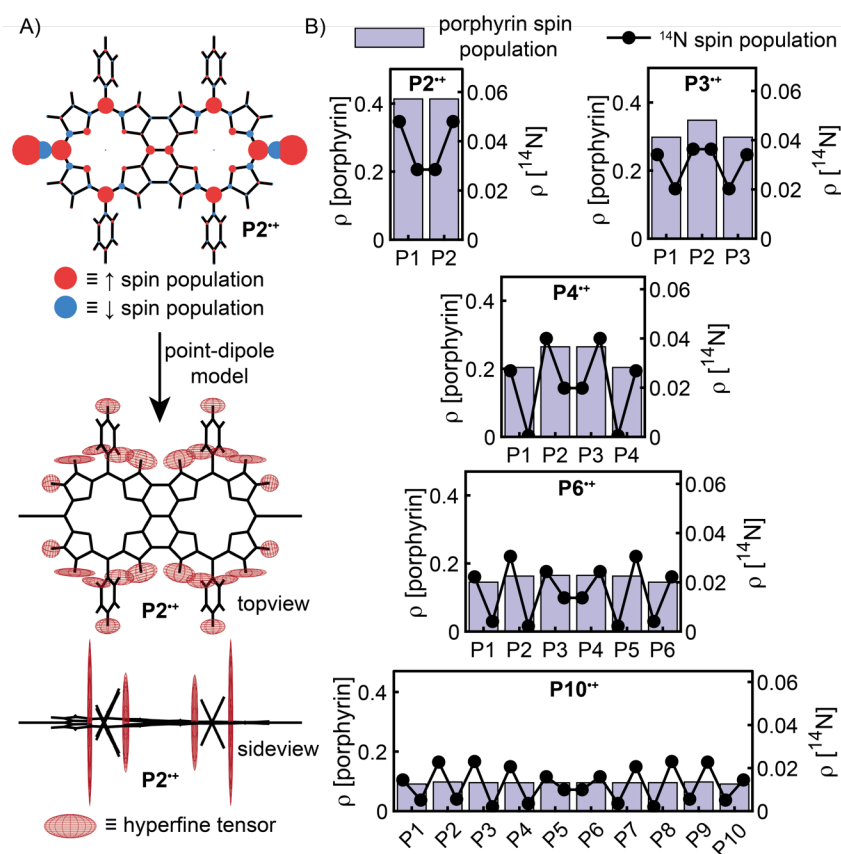

Figure 4. Modeling of hyperfine interactions
(A) Representation of the approach to derive the ^{1}H and ^{14}N hyperfine interactions of **P$N^{\bullet+}$** from their Mulliken spin populations with a distributed point-dipole model (exemplarily shown for **P2$^{\bullet+}$**). (B) Visualization of the spin populations ρ of each porphyrin unit (purple bars) and set of ^{14}N nuclei (black circles) used to calculate the hyperfine interactions in **P$N^{\bullet+}$** N = 2–4, 6, 10.

The surprising evolution of the ^{1}H Mims ENDOR spectra of **P$N^{\bullet+}$** can be explained by computational simulation. It is not feasible to simulate the EPR spectra of **P$N^{\bullet+}$** using DFT-calculated hyperfine tensors, due to the high computational cost of accurately calculating hyperfine interactions in molecules with more than four porphyrin units. To overcome this limitation, we calculated the hyperfine tensors directly from the spin density distributions in **P$N^{\bullet+}$** following the approach schematically summarized in Figure 4A and detailed in Section 4.3 of the Supplemental Information. In brief, we assigned a spin distribution to each oligomer guided by DFT-

calculated Mulliken spin populations that were systematically modified to account for the effects of solubilizing sidechains and silyl protecting groups omitted in the calculations. All assigned spin populations show full delocalization of the radical cations over all porphyrin units in each oligomer (Figure 4B and SI Figure S16). At the same time, the radical spin populations are non-uniformly distributed over the individual porphyrin units for $N \geq 2$, as exemplified by the ^{14}N spin populations in Figure 4B. The isotropic component of the hyperfine tensors is proportional to the spin on each nucleus, while the anisotropic component was calculated via a distributed point-dipole approximation of the dipolar electron-nuclear interactions typically used to obtain structural information from ENDOR measurements.[42,47,48] The full hyperfine tensors ^{14N}A and ^{1H}A obtained from this approach were employed in all simulations presented in this work (see SI Figures S17, S18 for a schematic visualization of the calculated hyperfine tensors).

The simulated ^{1}H and ^{14}N Mims ENDOR spectra of P$N^{\bullet+}$ (N = 1–4, 6, 10) shown in Figure 3A are in good agreement with the experimental spectra and qualitatively reproduce the trend in the experimental ENDOR *FWHM* as a function of oligomer length in Figure 3C. This is strong evidence for a coherent radical distribution over at least ten porphyrin units in P$N^{\bullet+}$ on the EPR time-scale in the frozen solution. The reason behind the discontinuous trend in the ^{1}H ENDOR *FWHM*, despite coherent delocalization over at least 10 porphyrin units in P$N^{\bullet+}$, becomes evident from the simulations of the individual hyperfine contributions to the ENDOR spectra (Figure 3A). For P1$^{\bullet+}$ and P2$^{\bullet+}$, the width of the ^{1}H ENDOR spectra is determined by the anisotropic hyperfine couplings to the *ortho*-protons of the aryl side groups, which decrease as expected from the monomer to the dimer. However, from the trimer onwards, the largest anisotropic hyperfine interactions switch from the *ortho*-protons to the inner β-protons of the terminal porphyrin units (β_3-protons), as shown schematically in Figure 3B. This is accompanied by the emergence of a resolved shoulder in the experimental ^{1}H ENDOR spectra that can be directly attributed to the β_3 hyperfine interactions in P$N^{\bullet+}$. Changes in the protons with the largest anisotropic hyperfine interactions can occur with increasing oligomer length, as illustrated by the ethyne-linked porphyrin radical cation oligomers.[22] The sustained increase in the β_3 hyperfine interactions in the terminal porphyrin units is however so far a unique feature of P$N^{\bullet+}$ and gives rise to the continuously increasing width of the ^{1}H ENDOR spectra. This increase is driven by a systematic redistribution of the spin density in the terminal porphyrin units with increasing oligomer length that locally overcompensates for the overall decrease of spin density per porphyrin with increasing radical delocalization (SI Figure S23). Ultimately, this change in the relative spin distribution, which is directly predicted by DFT calculations at the B3LYP/6-31G* level of theory, leads to larger anisotropic hyperfine contributions to ^{1H}A and consequently broader ^{1}H ENDOR spectra.

The hyperfine interactions in P14$^{\bullet+}$ and P18$^{\bullet+}$ were probed by W-band ^{1}H and ^{14}N Mims ENDOR spectroscopy in frozen solutions at 50 K and compared to the ENDOR spectra of P10$^{\bullet+}$ (SI Figure S27b). The ^{1}H ENDOR spectra of P14$^{\bullet+}$ measured at the $g_{x,y}$ and g_z field positions show a further increase in spectral width compared to P10$^{\bullet+}$, whereas the spectral shape and width of P14$^{\bullet+}$ and P18$^{\bullet+}$ are virtually identical. No significant changes in the width and shape of the ^{14}N ENDOR spectra of P$N^{\bullet+}$, N = 10, 14, 18 are evident within the signal to noise of the experimental data. This suggests a limit for coherent delocalization of the radical cation spin density between 10 and 14 porphyrin units in P$N^{\bullet+}$. Attempts to simulate the ENDOR spectra of P14$^{\bullet+}$ and P18$^{\bullet+}$ to precisely determine the effective delocalization length were not successful due to the unreliable description of the radical spin populations by DFT in these extended structures.
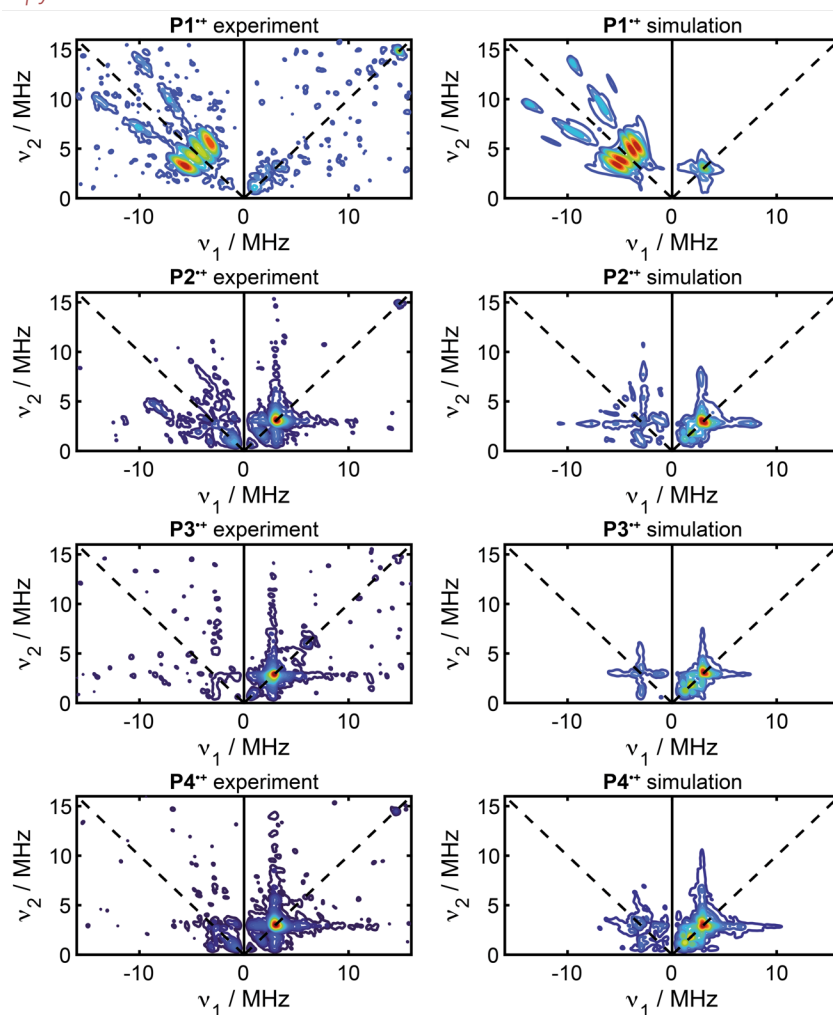
Figure 5. X-band ^{14}N HYSCORE spectroscopy
^{14}N HYSCORE spectra of **P1$^{•+}$** to **P4$^{•+}$** measured at 80 K in frozen CD$_2$Cl$_2$:toluene-d_8:THF-d_8 1:1:1 at X-band frequencies at field positions corresponding to $g_{x,y}$. The simulated spectra were obtained using anisotropic ^{14}N hyperfine tensors derived from distributed point-dipole calculations and ^{14}N quadrupole interactions calculated by DFT (B3LYP/EPR-II).

The anisotropic ^{14}N hyperfine interactions of **P$N^{•+}$** N = 1–4 were measured by HYSCORE spectroscopy at X-band frequencies to complement the study of the hyperfine interactions by Mims ENDOR spectroscopy (Figure 5). These measurements confirm the significant reduction in the nitrogen hyperfine couplings from **P1$^{•+}$** to **P2$^{•+}$**, as indicated by the shift of the strongest signal contributions from the (−,+) to the (+,+) quadrant of the HYSCORE spectra. This trend continues for the HYSCORE spectrum of **P3$^{•+}$** with a further reduced signal in the (−,+) quadrant followed by a slightly higher spectral contribution in the (−,+) quadrant for **P4$^{•+}$**. Simulations of the HYSCORE spectra using nitrogen hyperfine tensors obtained via the distributed point-dipole approximation are in good agreement with the experimental spectra. This provides additional evidence for the coherent delocalization of the radical spin density over at least four porphyrin units in **P$N^{•+}$**. In addition, the substantially better agreement of these simulations with the experiment compared to simulations with DFT calculated hyperfine interactions further strengths the validity of the hyperfine tensors calculated via the distributed point-dipole approximation (SI Figure S24). The simulated spectra also reproduce the experimentally observed trend of a continuously reduced signal in the (−,+) quadrant for N = 1–3 followed by a slight increase for N = 4 caused by an initial reduction of the largest out-of-plane nitrogen hyperfine coupling from 11.7 MHz in **P1$^{•+}$** to 4.96 MHz in **P3$^{•+}$** followed by an increase to 5.47 MHz in **P4$^{•+}$** (SI Table S6). This is further experimental evidence for the non-uniform spin density distribution in **P$N^{•+}$**.

Accidental Oxidation of Extended Porphyrin Nanoribbons

The characterization of the edge-fused porphyrin nanoribbons **P***N* by solution-phase ^{1}H NMR spectroscopy shows a substantial broadening of the proton resonances for *N* > 4 (SI Figure S25b), as previously reported by Osuka.[26,49] This prompted us to investigate samples of **P***N* prior to chemical oxidation by EPR spectroscopy. Cw-EPR spectra of **P2**, **P6**, and **P10** at room temperature and X-band frequencies without chemical oxidation confirm the closed-shell, diamagnetic character of **P2** and the emergence of increasing amounts of an EPR active, paramagnetic species in **P6** and **P10** (SI Figure S25a). Quantification of the radical content of the samples before and after chemical oxidation with BAHA by changes in the double-integrals of their cw-EPR spectra confirms that about 2% of **P6** and 12% of **P10** form radicals under ambient conditions. The nature of these radicals was investigated by a combination of room temperature X-band cw-EPR and W-band pulse EPR spectroscopy in a frozen solution at 50 K (SI Figure S26). The cw-EPR spectra and echo-detected field sweep spectra of **P6** and **P10** both exhibit identical spectral shapes and *g*-anisotropies with and without chemical oxidation. In addition, both species have identical anisotropic proton hyperfine interactions as confirmed by the identical width and shape of their [1]H Mims ENDOR spectra measured at field positions corresponding to $g_{x,y}$ and g_z. In combination, this spectroscopic evidence demonstrates that the partial open-shell character of **P6** and **P10** prior to chemical oxidation results from the spontaneous formation of radical cations, presumable due to aerobic oxidation. No degradation of the partially oxidized samples was observed during purification by silica and size-exclusion chromatography or while they were stored as solid samples. Due to their even further extended π-systems, **P14** and **P18** exist predominantly as radical cations after exposure to air under ambient conditions. The formation of the radical cations shifts the absorption spectra to longer wavelengths, as discussed in the next section (Figure 6).

Optical vis-NIR-MIR Spectroelectrochemistry

Optical spectroscopy of organic mixed valence compounds such as **P***N*•+ provides important information about their reorganization energy λ and electronic coupling energy H, and probes the polaron delocalization on a fs-time-scale in solution.[3,50] A simple model to describe polaron delocalization is the Marcus–Hush theory briefly summarized in Section 5.1 of the Supplemental Information.[51,52] In this theoretical framework, the extent of polaron delocalization is determined by the ratio of the electronic coupling H and the reorganization energy λ and allows for the classification of mixed valence compounds into three categories: *i*) the electronic coupling between the individual sites is weak ($H \approx 0$) and the charge is predominantly localized on one site of the system (Robin–Day class I); *ii*) the electronic coupling is significant ($0 < 2H < \lambda$) resulting in partial charge delocalization (Robin–Day class II); iii) the electronic coupling is so strong ($2H > \lambda$) that it leads to complete charge delocalization (Robin–Day class III) (SI Figure S28).[3,53] Compared to their neutral analogues, radical cations of π-conjugated oligomers typically feature two characteristic low energy absorption bands P_1 and P_2 in their optical absorption spectra which approximately correspond to HOMO → SOMO and SOMO → LUMO transitions, respectively (SI Figure S29).[54-56]
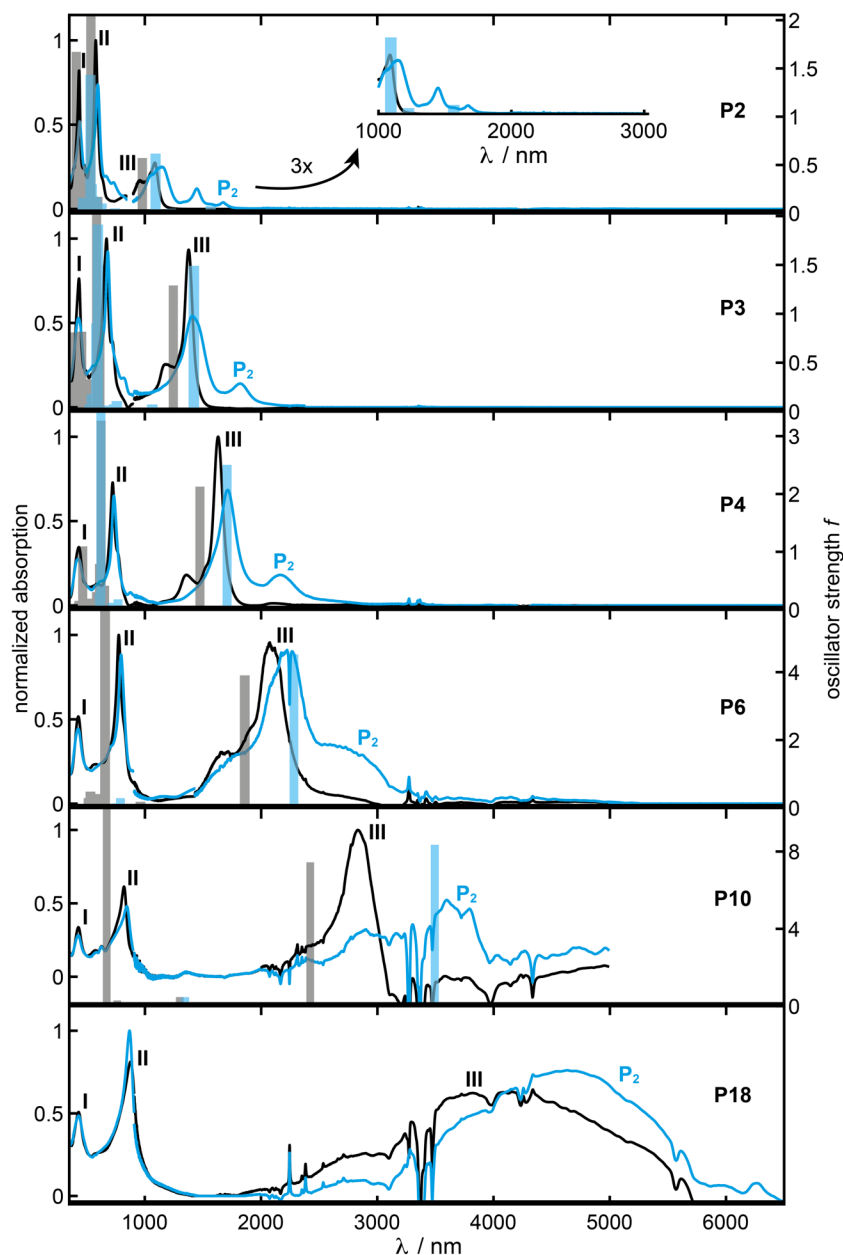
Figure 6. Vis-NIR-MIR spectra of neutral and oxidized porphyrin oligomers

Vis-NIR-MIR normalized absorption spectra of **P***N* (black) and **P***N*•+ (blue) from spectroelectrochemistry in CH₂Cl₂ (0.1 M Bu₄NPF₆, 298 K). The vertical bars indicate the TD-DFT (LC-ωHPBE/6-31G*; ω = 0.1) calculated wavelengths and oscillator strengths *f* for the electronic transitions of the neutral and oxidized oligomers. Attempts to perform TD-DFT calculations for **P18** and **P18**•+ were unsuccessful due to the extensive computational requirement.

The vis-NIR-MIR absorption spectra of **P***N* were measured as a function of electrochemical oxidation in CH₂Cl₂ containing Bu₄NPF₆ (0.1 M) as electrolyte under an argon atmosphere. Deconvolution of the raw data gave the absorption spectra of several different oxidation states in each oligomer (SI Figure S30). Square wave voltammetry of **P***N* *N* = 2–4, 6 shows a continuous decrease of the first oxidation potential with increasing oligomer length (SI Figure S35). The absorption spectra of neutral and oxidized oligomers **P2** to **P4**, **P6**, **P10**, and **P18** obtained from spectroelectrochemistry are shown in Figure 6. The spectra of the neutral oligomers shown here are under slight electrochemical reduction to avoid the accidental oxidation observed under aerobic conditions. The absorption spectra of neutral **P***N* exhibit three characteristic peaks I, II, and III that originate from the *B*y, *B*x, and *Q*x transitions of a porphyrin monomer, respectively.[27] TD-DFT calculations of **P***N* with LC-ωHPBE (ω = 0.1) as functional indicate that band III arises from the HOMO → LUMO transition in each neutral oligomer in agreement with previous reports.[26,27,49] The absorption spectra of the radical cations **P***N*•+ each exhibit an additional low energy absorption peak. This contrasts with the previously reported optical

10

signatures of oxidized butadiyne-linked porphyrin oligomers which feature two distinct electronic transitions: P_1 at 2000–5000 nm and P_2 at around 1000 nm.[35] TD-DFT calculation of the excitation energies of **PN** and **PN$^{•+}$** (N = 1–4, 6, 10) at the LC-ωHPBE/6-31G* (ω = 0.1) level of theory are in good agreement with the experimental observations (Figures 6 and 7). Attempts to perform TD-DFT calculations for **P18** and **P18$^{•+}$** were unsuccessful due to the extensive computational requirement. Comparison of the calculated electronic transitions to those observed in the deconvoluted experimental spectra suggest that the characteristic low energy absorption bands of **PN$^{•+}$** mainly arise from SOMO → LUMO transitions and therefore correspond to the P_2 bands of the hole polarons. The P_1 bands of **PN$^{•+}$** are dipole forbidden, merged with the SOMO → LUMO transition, or occur at relatively higher excitation energies depending on the length of the oligomer and functional employed in the TD-DFT calculations. Therefore, we focus on the P_2 bands for the following analysis.
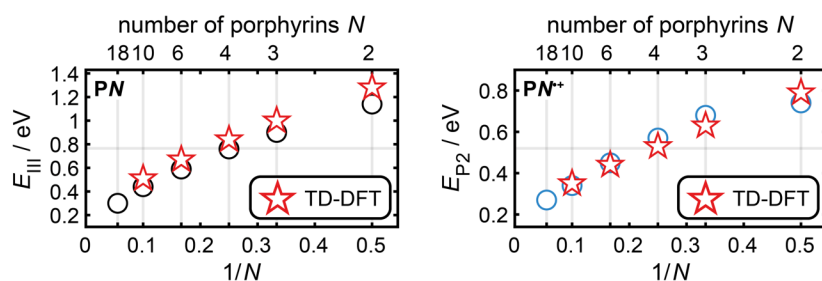

Figure 7. Trend in the long-wavelength absorption energies
Trend in the experimental and TD-DFT (LC-ωHPBE/6-31G*; ω = 0.1) calculated transition energies E for the lowest energy absorption bands of **PN** and the P_2 bands in **PN$^{•+}$** in CH_2Cl_2.

The lowest energy absorption bands (III) of **PN** and P_2 bands of **PN$^{•+}$** exhibit a continuous bathochromic shift with increasing oligomer length which is replicated by TD-DFT calculations and consistent with a continuous narrowing of their optical excitation gaps (Figure 7, SI Table S7). This trend fits a particle-in-a-box model, as shown in Supplemental Figure S31. For the neutral oligomers **PN**, the experimental trend and fit both show that the progressive bathochromic shift of band III does not saturate for $N \leq 18$ which suggests an effective conjugation length $N_{eff} \geq 18$ porphyrin units. In contrast, Osuka reported an effective conjugation length of 14–16 porphyrin units for **PN**.[49] The radical cation P_2 bands shows a similar trend to band III in the neutral oligomers, although with a clear shift to lower energies over the entire oligomer series. This points towards a limit of coherent radical delocalization beyond 18 porphyrin units in **PN$^{•+}$**.

To describe electron transfer processes in molecular chains comprised of N repeat units, Rathore and co-workers developed the multistate parabolic model (MPM) which extends the Marcus–Hush theory of mixed valence systems to an arbitrary number of electron transfer sites (see SI Section 5.3).[57] Modelling of the trend in the experimental P_2 excitation energies E_{P2} for **PN$^{•+}$** N = 3, 4, 6, 10, 18 with the MPM Hamiltonian gives an electronic coupling H/λ = 8.3 between neighboring porphyrin units (SI Figure S32). This implies that porphyrin nanoribbon radical cations **PN$^{•+}$** are best described as Robin–Day class III mixed valence compounds. However, beyond this qualitative classification the multistate parabolic model struggles to accurately describe the electronic structure of the extended porphyrin oligomer cations which suggests a limited suitability of the MPM approximation for electron transfer processes in very strongly coupled oligomers.

Discussion and Summary

We have investigated the extent of delocalization in the radical cations of a series of $\beta,meso,\beta$-triply linked porphyrin oligomers **PN** by a combination of EPR and optical spectroscopy and supporting DFT simulations. Cw-EPR spectroscopy at room temperature in solution, together with ^{1}H and ^{14}N Mims ENDOR spectroscopy in frozen solutions at 50 K, demonstrate coherent polaron delocalization over 10 to 14 porphyrin units in **PN$^{•+}$**. These conclusions have been guided by simulations of the experimental spectra using ^{1}H and ^{14}N hyperfine interactions calculated from a fully delocalized spin density distribution in each oligomer via a distributed point-dipole approximation. The versatility and accuracy of this approach is highlighted by the fact that all cw-EPR spectra, ^{1}H and ^{14}N ENDOR spectra, and, where applicable, ^{14}N HYSCORE spectra, of an oligomer could be simulated with the same set of hyperfine interactions. The simulations also demonstrate that the deviation of the cw-EPR spectral width from an ideal Norris trend and the discontinuous trend in the ^{1}H ENDOR full width at half maximum result from a non-uniform spin density distribution and local redistributions of spin density and do not contradict a full delocalization of the radical spin density. This highlights the importance of theoretical modelling to guide the interpretation of experimental EPR results and that discussions based merely on trends in the experimental spectra are insufficient to determine the delocalization of organic radicals. The continuous bathochromic shift of the P_2 lowest energy absorption band in the vis-NIR-MIR absorption spectra of **PN$^{•+}$** in combination with TD-DFT calculations suggest

an effective polaron delocalization length of more than 18 porphyrin units in $PN^{\bullet+}$. In conclusion, the combined spectroscopic analysis clearly shows radical cation delocalization over more than 10 porphyrins in $PN^{\bullet+}$. This corresponds to an effective polaron delocalization length greater than 8.5 nm and marks, to the best of our knowledge, the longest coherent polaron delocalization reported in π-conjugated molecular materials to date.[20,22,33] For comparison, the polaron coherence length in poly(3-hexylthiophene) (P3HT) is approximately 4–7 repeat units, which corresponds to 1.5–2.7 nm.[58,59] These long delocalization lengths combined with the increasing coherence times in extended oligomers show that porphyrin nanoribbons are exceptionally effective molecular wires.

EXPERIMENTAL PROCEDURES

Resource availability

Lead contact
Further information and requests for resources should be directed to and will be fulfilled by the lead contact, Christiane Timmel (christiane.timmel@chem.ox.ac.uk).

Materials availability
The materials generated are available from the lead contact upon reasonable request.

Data and code availability
All data supporting the conclusions of this study are available in the main text and supplemental information or from the lead contact upon reasonable request.

SUPPLEMENTAL INFORMATION

Supplemental information can be found online.

ACKNOWLEDGMENTS

AUTHOR CONTRIBUTIONS

S.M.K., J.-R.D., H.L.A., and C.R.T. conceived the project. J.-R.D. conducted the synthesis and chemical characterization. H.G. assisted with the chemical characterization. S.M.K. carried out X-band cw and W-band pulse EPR measurements and analyzed and simulated all EPR results. A.J.R. assisted with measurements at W-band frequencies and performed the HYSCORE measurements. S.M.K., J.-R.D., and R.M.J.J. performed the spectroelectrochemistry (SEC) measurements. S.M.K. analyzed the SEC data. J.-R.D. measured the redox potentials of **P2**–**P6**. S.M.K. and J.-R.D. performed the theoretical calculations. H.L.A and C.R.T. coordinated and supervised the project. S.M.K., H.L.A., and C.R.T. wrote the manuscript. All authors contributed to the refinement of the manuscript.

DECLARATION OF INTERESTS

The authors declare no competing interests.

Inclusion and Diversity

We support inclusive, diverse, and equitable conduct of research.

REFERENCES

1. Bredas, J.L., and Street, G.B. (1985). Polarons, bipolarons, and solitons in conducting polymers. Accounts of chemical research *18*, 309-315.
2. Coropceanu, V., Cornil, J., da Silva Filho, D.A., Olivier, Y., Silbey, R., and Brédas, J.-L. (2007). Charge Transport in Organic Semiconductors. Chemical Reviews *107*, 926-952. 10.1021/cr050140x.
3. Heckmann, A., and Lambert, C. (2012). Organic Mixed-Valence Compounds: A Playground for Electrons and Holes. Angewandte Chemie International Edition *51*, 326-392. https://doi.org/10.1002/anie.201100944.

4.   Campbell, D.K., Bishop, A.R., and Fesser, K. (1982). Polarons in quasi-one-dimensional systems. Physical Review B *26*, 6862-6874. 10.1103/PhysRevB.26.6862.

5.   Sakanoue, T., and Sirringhaus, H. (2010). Band-like temperature dependence of mobility in a solution-processed organic semiconductor. Nature Materials *9*, 736-740. 10.1038/nmat2825.

6.   Bässler, H., and Köhler, A. (2012). Charge Transport in Organic Semiconductors. In Unimolecular and Supramolecular Electronics I: Chemistry and Physics Meet at Metal-Molecule Interfaces, R.M. Metzger, ed. (Springer Berlin Heidelberg), pp. 1-65. 10.1007/128_2011_218.

7.   Bakulin, A.A., Rao, A., Pavelyev, V.G., van Loosdrecht, P.H.M., Pshenichnikov, M.S., Niedzialek, D., Cornil, J., Beljonne, D., and Friend, R.H. (2012). The Role of Driving Energy and Delocalized States for Charge Separation in Organic Semiconductors. Science *335*, 1340-1344. doi:10.1126/science.1217745.

8.   Tamura, H., and Burghardt, I. (2013). Ultrafast Charge Separation in Organic Photovoltaics Enhanced by Charge Delocalization and Vibronically Hot Exciton Dissociation. Journal of the American Chemical Society *135*, 16364-16367. 10.1021/ja4093874.

9.   Ghosh, R., and Spano, F.C. (2020). Excitons and Polarons in Organic Materials. Accounts of Chemical Research *53*, 2201-2211. 10.1021/acs.accounts.0c00349.

10.   Moser, M., Savva, A., Thorley, K., Paulsen, B.D., Hidalgo, T.C., Ohayon, D., Chen, H., Giovannitti, A., Marks, A., Gasparini, N., et al. (2021). Polaron Delocalization in Donor–Acceptor Polymers and its Impact on Organic Electrochemical Transistor Performance. Angewandte Chemie International Edition *60*, 7777-7785. https://doi.org/10.1002/anie.202014078.

11.   Matheson, A.B., Ruseckas, A., Pearson, S.J., and Samuel, I.D.W. (2019). Hole delocalization as a driving force for charge pair dissociation in organic photovoltaics. Materials Horizons *6*, 1050-1056. 10.1039/C8MH01204K.

12.   Niklas, J., Zheng, T., Neshchadin, A., Mardis, K.L., Yu, L., and Poluektov, O.G. (2020). Polaron and Exciton Delocalization in Oligomers of High-Performance Polymer PTB7. Journal of the American Chemical Society *142*, 1359-1366. 10.1021/jacs.9b10859.

13.   Schott, S., Chopra, U., Lemaur, V., Melnyk, A., Olivier, Y., Di Pietro, R., Romanov, I., Carey, R.L., Jiao, X., Jellett, C., et al. (2019). Polaron spin dynamics in high-mobility polymeric semiconductors. Nature Physics *15*, 814-822. 10.1038/s41567-019-0538-0.

14.   Watanabe, S., Ando, K., Kang, K., Mooser, S., Vaynzof, Y., Kurebayashi, H., Saitoh, E., and Sirringhaus, H. (2014). Polaron spin current transport in organic semiconductors. Nature Physics *10*, 308-313. 10.1038/nphys2901.

15.   Tsurumi, J., Matsui, H., Kubo, T., Häusermann, R., Mitsui, C., Okamoto, T., Watanabe, S., and Takeya, J. (2017). Coexistence of ultra-long spin relaxation time and coherent charge transport in organic single-crystal semiconductors. Nature Physics *13*, 994-998. 10.1038/nphys4217.

16.   Bullard, G., Tassinari, F., Ko, C.-H., Mondal, A.K., Wang, R., Mishra, S., Naaman, R., and Therien, M.J. (2019). Low-Resistance Molecular Wires Propagate Spin-Polarized Currents. Journal of the American Chemical Society *141*, 14707-14711. 10.1021/jacs.9b06142.

17.   Hines, T., Diez-Perez, I., Hihath, J., Liu, H., Wang, Z.-S., Zhao, J., Zhou, G., Müllen, K., and Tao, N. (2010). Transition from Tunneling to Hopping in Single Molecular Junctions by Measuring Length and Temperature Dependence. Journal of the American Chemical Society *132*, 11658-11664. 10.1021/ja1040946.

18.   Lu, Q., Liu, K., Zhang, H., Du, Z., Wang, X., and Wang, F. (2009). From Tunneling to Hopping: A Comprehensive Investigation of Charge Transport Mechanism in Molecular Junctions Based on Oligo(p-phenylene ethynylene)s. ACS Nano *3*, 3861-3868. 10.1021/nn9012687.

19.   Chen, Z., Deng, J.-R., Hou, S., Bian, X., Swett, J.L., Wu, Q., Baugh, J., Bogani, L., Briggs, G.A.D., Mol, J.A., et al. (2023). Phase-Coherent Charge Transport through a Porphyrin Nanoribbon. Journal of the American Chemical Society *145*, 15265-15274. 10.1021/jacs.3c02451.

20.   Rawson, J., Angiolillo, P.J., and Therien, M.J. (2015). Extreme electron polaron spatial delocalization in π-conjugated materials. Proceedings of the National Academy of Sciences *112*, 13779-13783. 10.1073/pnas.1512318112.

21.   Rawson, J., Angiolillo, P.J., Frail, P.R., Goodenough, I., and Therien, M.J. (2015). Electron Spin Relaxation of Hole and Electron Polarons in π-Conjugated Porphyrin Arrays: Spintronic Implications. The Journal of Physical Chemistry B *119*, 7681-7689. 10.1021/jp5122728.

22.   Moise, G., Tejerina, L., Rickhaus, M., Anderson, H.L., and Timmel, C.R. (2019). Spin Delocalization in the Radical Cations of Porphyrin Molecular Wires: A New Perspective on EPR Approaches. The Journal of Physical Chemistry Letters *10*, 5708-5712. 10.1021/acs.jpclett.9b02262.

23.   Susumu, K., Frail, P.R., Angiolillo, P.J., and Therien, M.J. (2006). Conjugated Chromophore Arrays with Unusually Large Hole Polaron Delocalization Lengths. Journal of the American Chemical Society *128*, 8380-8381. 10.1021/ja0614823.

24.   Bruce, R.C., Wang, R., Rawson, J., Therien, M.J., and You, W. (2016). Valence Band Dependent Charge Transport in Bulk Molecular Electronic Devices Incorporating Highly Conjugated Multi-[(Porphinato)Metal] Oligomers. Journal of the American Chemical Society *138*, 2078-2081. 10.1021/jacs.5b10772.

25.   Li, Z., Park, T.-H., Rawson, J., Therien, M.J., and Borguet, E. (2012). Quasi-Ohmic Single Molecule Charge Transport through Highly Conjugated meso-to-meso Ethyne-Bridged Porphyrin Wires. Nano Letters *12*, 2722-2727. 10.1021/nl2043216.

26.   Tsuda, A., and Osuka, A. (2001). Fully Conjugated Porphyrin Tapes with Electronic Absorption Bands That Reach into Infrared. Science *293*, 79-82. 10.1126/science.1059552.

27.   Cho, H.S., Jeong, D.H., Cho, S., Kim, D., Matsuzaki, Y., Tanaka, K., Tsuda, A., and Osuka, A. (2002). Photophysical Properties of Porphyrin Tapes. Journal of the American Chemical Society *124*, 14642-14654. 10.1021/ja020826w.

28.   Tanaka, T., and Osuka, A. (2015). Conjugated porphyrin arrays: synthesis, properties and applications for functional materials. Chemical Society Reviews *44*, 943-969. 10.1039/C3CS60443H.

29.   Sedghi, G., Esdaile, L.J., Anderson, H.L., Martin, S., Bethell, D., Higgins, S.J., and Nichols, R.J. (2012). Comparison of the Conductance of Three Types of Porphyrin-Based Molecular Wires: **β**,meso,**β**-Fused Tapes, meso-Butadiyne-Linked and Twisted meso-meso Linked Oligomers. Advanced Materials *24*, 653-657. https://doi.org/10.1002/adma.201103109.

30.   Leary, E., Limburg, B., Alanazy, A., Sangtarash, S., Grace, I., Swada, K., Esdaile, L.J., Noori, M., González, M.T., Rubio-Bollinger, G., et al. (2018). Bias-Driven Conductance Increase with Length in Porphyrin Tapes. Journal of the American Chemical Society *140*, 12877-12883. 10.1021/jacs.8b06338.

31.   Algethami, N., Sadeghi, H., Sangtarash, S., and Lambert, C.J. (2018). The Conductance of Porphyrin-Based Molecular Nanowires Increases with Length. Nano Letters *18*, 4482-4486. 10.1021/acs.nanolett.8b01621.

32. Thomas, J.O., Sowa, J.K., Limburg, B., Bian, X., Evangeli, C., Swett, J.L., Tewari, S., Baugh, J., Schatz, G.C., Briggs, G.A.D., et al. (2021). Charge transport through extended molecular wires with strongly correlated electrons. Chemical Science *12*, 11121-11129. 10.1039/D1SC03050G.

33. Thorley, K.J. (2023). Estimation of Polaron Delocalization Lengths in Conjugated Organic Polymers. The Journal of Physical Chemistry B *127*, 5102-5114. 10.1021/acs.jpcb.3c00153.

34. Grozema, F.C., Houarner-Rassin, C., Prins, P., Siebbeles, L.D.A., and Anderson, H.L. (2007). Supramolecular Control of Charge Transport in Molecular Wires. Journal of the American Chemical Society *129*, 13370-13371. 10.1021/ja0751274.

35. Peeks, M.D., Tait, C.E., Neuhaus, P., Fischer, G.M., Hoffmann, M., Haver, R., Cnossen, A., Harmer, J.R., Timmel, C.R., and Anderson, H.L. (2017). Electronic Delocalization in the Radical Cations of Porphyrin Oligomer Molecular Wires. Journal of the American Chemical Society *139*, 10461-10471. 10.1021/jacs.7b05386.

36. Norris, J.R., Uphaus, R.A., Crespi, H.L., and Katz, J.J. (1971). Electron Spin Resonance of Chlorophyll and the Origin of Signal I in Photosynthesis. Proceedings of the National Academy of Sciences *68*, 625-628. 10.1073/pnas.68.3.625.

37. McConnell, H.M. (1956). Indirect Hyperfine Interactions in the Paramagnetic Resonance Spectra of Aromatic Free Radicals. The Journal of Chemical Physics *24*, 764-766. 10.1063/1.1742605.

38. Cohen, A.J., Mori-Sánchez, P., and Yang, W. (2008). Insights into Current Limitations of Density Functional Theory. Science *321*, 792-794. doi:10.1126/science.1158722.

39. Kaupp, M., Renz, M., Parthey, M., Stolte, M., Würthner, F., and Lambert, C. (2011). Computational and spectroscopic studies of organic mixed-valence compounds: where is the charge? Physical Chemistry Chemical Physics *13*, 16973-16986. 10.1039/C1CP21772K.

40. Renz, M., Theilacker, K., Lambert, C., and Kaupp, M. (2009). A Reliable Quantum-Chemical Protocol for the Characterization of Organic Mixed-Valence Compounds. Journal of the American Chemical Society *131*, 16292-16302. 10.1021/ja9070859.

41. Walton, J.C. (2012). Analysis of Radicals by EPR. In Encyclopedia of Radicals in Chemistry, Biology and Materials. https://doi.org/10.1002/9781119953678.rad001.

42. Schweiger, A., and Jeschke, G. (2001). Principles of pulse electron paramagnetic resonance (Oxford University Press).

43. Rohrer, M., Gast, P., Möbius, K., and Prisner, T.F. (1996). Anisotropic motion of semiquinones in photosynthetic reaction centers of Rhodobacter sphaeroides R26 and in frozen isopropanol solution as measured by pulsed high-field EPR at 95 GHz. Chemical Physics Letters *259*, 523-530. https://doi.org/10.1016/0009-2614(96)00822-6.

44. Bagryanskaya, E.G., Polovyanenko, D.N., Fedin, M.V., Kulik, L., Schnegg, A., Savitsky, A., Möbius, K., Coleman, A.W., Ananchenko, G.S., and Ripmeester, J.A. (2009). Multifrequency EPR study of the mobility of nitroxides in solid-state calixarene nanocapsules. Physical Chemistry Chemical Physics *11*, 6700-6707. 10.1039/B906827A.

45. Jackson, C.E., Lin, C.-Y., van Tol, J., and Zadrozny, J.M. (2020). Orientation dependence of phase memory relaxation in the V(IV) ion at high frequencies. Chemical Physics Letters *739*, 137034. https://doi.org/10.1016/j.cplett.2019.137034.

46. Wilson, T.M., Hori, T., Yoon, M.-C., Aratani, N., Osuka, A., Kim, D., and Wasielewski, M.R. (2010). Rapid Intramolecular Hole Hopping in meso−meso and meta-Phenylene Linked Linear and Cyclic Multiporphyrin Arrays. Journal of the American Chemical Society *132*, 1383-1388. 10.1021/ja908605s.

47. Meyer, A., Dechert, S., Dey, S., Höbartner, C., and Bennati, M. (2020). Measurement of Angstrom to Nanometer Molecular Distances with 19F Nuclear Spins by EPR/ENDOR Spectroscopy. Angewandte Chemie International Edition *59*, 373-379. https://doi.org/10.1002/anie.201908584.

48. Atherton, N.M., and Shackleton, J.F. (1984). Proton hyperfine couplings in VO(H2O)2+5: The validity of the point-dipole approximation. Chemical Physics Letters *103*, 302-304. https://doi.org/10.1016/0009-2614(84)80011-1.

49. Ikeda, T., Aratani, N., and Osuka, A. (2009). Synthesis of Extremely π-Extended Porphyrin Tapes from Hybrid meso-meso Linked Porphyrin Arrays: An Approach Towards the Conjugation Length. Chemistry – An Asian Journal *4*, 1248-1256. 10.1002/asia.200900125.

50. Brunschwig, B.S., Creutz, C., and Sutin, N. (2002). Optical transitions of symmetrical mixed-valence systems in the Class II–III transition regime. Chemical Society Reviews *31*, 168-184. 10.1039/B008034I.

51. Hush, N.S. (1985). Distance Dependence of Electron Transfer Rates. Coordination Chemistry Reviews *64*, 135-157. https://doi.org/10.1016/0010-8545(85)80047-3.

52. Hush, N.S. (1968). Homogeneous and heterogeneous optical and thermal electron transfer. Electrochimica Acta *13*, 1005-1023. https://doi.org/10.1016/0013-4686(68)80032-5.

53. Robin, M.B., and Day, P. (1968). Mixed Valence Chemistry-A Survey and Classification. In Advances in Inorganic Chemistry and Radiochemistry, H.J. Emeléus, and A.G. Sharpe, eds. (Academic Press), pp. 247-422. https://doi.org/10.1016/S0065-2792(08)60179-X.

54. Heimel, G. (2016). The Optical Signature of Charges in Conjugated Polymers. ACS Central Science *2*, 309-315. 10.1021/acscentsci.6b00073.

55. Lane, P.A., Wei, X., and Vardeny, Z.V. (1996). Studies of Charged Excitations in $\mathit{\ensuremath{\pi}}$-Conjugated Oligomers and Polymers by Optical Modulation. Physical Review Letters *77*, 1544-1547. 10.1103/PhysRevLett.77.1544.

56. Wohlgenannt, M. (2004). Polarons in π-conjugated semiconductors: absorption spectroscopy and spin-dependent recombination. physica status solidi (a) *201*, 1188-1204. https://doi.org/10.1002/pssa.200404331.

57. Talipov, M.R., Boddeda, A., Timerghazin, Q.K., and Rathore, R. (2014). Key Role of End-Capping Groups in Optoelectronic Properties of Poly-p-phenylene Cation Radicals. The Journal of Physical Chemistry C *118*, 21400-21408. 10.1021/jp5082752.

58. Ghosh, R., Chew, A.R., Onorato, J., Pakhnyuk, V., Luscombe, C.K., Salleo, A., and Spano, F.C. (2018). Spectral Signatures and Spatial Coherence of Bound and Unbound Polarons in P3HT Films: Theory Versus Experiment. The Journal of Physical Chemistry C *122*, 18048-18060. 10.1021/acs.jpcc.8b03873.

59. Stanfield, D.A., Mehmedović, Z., and Schwartz, B.J. (2021). Vibrational Stark Effect Mapping of Polaron Delocalization in Chemically Doped Conjugated Polymers. Chemistry of Materials *33*, 8489-8500. 10.1021/acs.chemmater.1c02934.